Relationships between Water Vapor Path and Precipitation over the Tropical Oceans

CHRISTOPHER S. BRETHERTON

Department of Atmospheric Sciences, University of Washington, Seattle, Washington

MATTHEW E. PETERS

Department of Applied Mathematics, University of Washington, Seattle, Washington

LARISSA E. BACK

Department of Atmospheric Sciences, University of Washington, Seattle, Washington

(Manuscript received 14 August 2003, in final form 17 October 2003)

ABSTRACT

The relationship between water vapor path W and surface precipitation rate P over tropical oceanic regions is analyzed using 4 yr of gridded daily SSM/I satellite microwave radiometer data. A tight monthly mean relationship P (mm day^{-1}) = exp[11.4(r − 0.522)] for all tropical ocean regions and seasons is found between P and a column-relative humidity r obtained by dividing W by the corresponding saturation water vapor path. A similar relation, albeit with more scatter, also holds at daily time scales, and can be interpreted as a moisture adjustment time scale of 12 h for convective rainfall to affect humidity anomalies on 300-km space scales. Cross-spectral analysis shows statistically significant covariability of actual and r-predicted precipitation at all frequencies, with negligible phase lag. The correlation of actual and r-predicted precipitation exceeds 0.5 on intraseasonal and longer time scales.

The SSM/I retrievals of W and P are found to be skillful even at daily time scales when compared with in situ radiosonde and radar-derived area-averaged precipitation data from Kwajalein Island, but the microwave estimates of daily P scatter considerably about the radar estimates (which are considered to be more reliable). Using the radar-derived precipitation in combination with microwave-derived W yields a daily r–P relationship at Kwajalein similar to that derived solely from microwave measurements, but with somewhat less P associated with the highest values of r. This emphasizes that the absolute calibration of the r–P relationship is somewhat dependent on the datasets used to derive r and especially P. Nevertheless, the results provide a useful constraint on conceptual models and parameterizations of tropical deep convection.

1. Introduction

As known to scientists and nonscientists alike, it tends to be humid when and where there is sustained deep convective rainfall. Raymond (2000) even investigated the large-scale dynamical consequences of a bulk parameterization of tropical rainfall rate P in terms of a vertically integrated moisture deficit from saturation. However, there has been comparatively little quantitative investigation of the relation of P to humidity and its vertical structure, and how this relationship depends on the time and space scales under consideration.

Analyses of radiosonde data from various tropical locations have shown that episodes of deep convection are followed by increases in mid- to upper-tropospheric relative humidity, while a relatively moist low- to mid-troposphere helps initiate tropical deep convection (e.g., Numaguti et al. 1995; Ushiyama et al. 1995; Yoneyama and Fujitani 1995; Johnson and Lin 1997; Brown and Zhang 1997; Sherwood 1999; Sherwood and Wahrlich 1999; Sobel et al. 2004). Zeng (1999) showed how supplementary use of satellite-derived column water vapor path W could be used to improve predictions of tropical rainfall from infrared brightness temperature.

The data analyzed by these authors did not permit them to attempt a comprehensive observational assessment of relationships between P and humidity on different time scales. In this study, we use 4 years of daily microwave retrievals of P and W over the entire tropical ocean to examine this issue—enough samples in time and space to clearly identify any correlation between these variables. At daily time scales, P (and to a lesser extent W) are undersampled at any location and subject to potentially serious retrieval biases; to test their robustness we use a dataset including several months of radiosonde and ground-based radar-derived area-aver-

Corresponding author address: Christopher S. Bretherton, Department of Atmospheric Sciences, University of Washington, Box 351640, Seattle, WA 98195-1640.
E-mail: breth@atmos.washington.edu

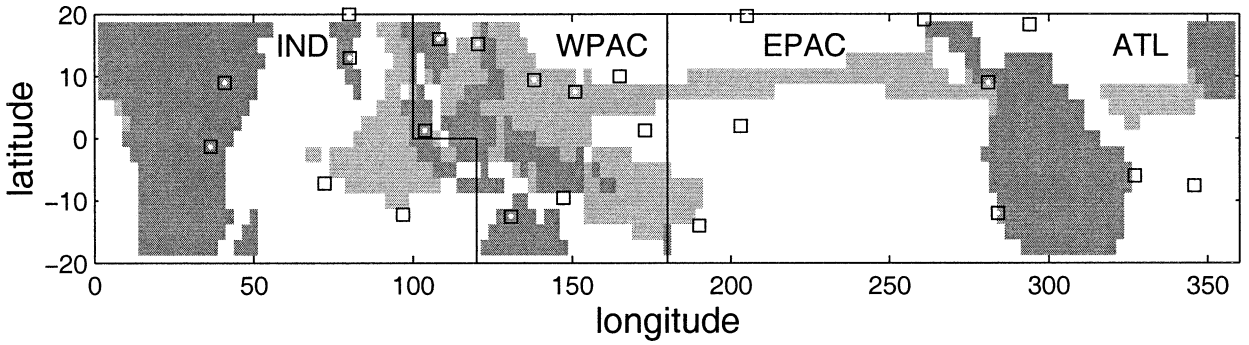

FIG. 1. The four tropical ocean analysis regions (labeled and separated by land or solid black lines) and tropical radiosonde sites used in this paper (squares). Light shading indicates regions where SSM/I-derived 1998–2001 average precipitation exceeded 8 mm day^{-1}. Dark shading indicates land grid points.

aged precipitation measurements centered on Kwajalein Island in the central Pacific ITCZ.

2. Data description

We obtained retrievals of P and W (retrieval algorithm version 5) from Remote Sensing Systems Inc. (more information available online at http://www.remss.com) for all available Special Sensor Microwave Imager [(SSM/I) on Defense Meteorological Satellite Program (DMSP) satellites *F10*, *F11*, *F12*, and *F14*, 1400-km-wide swaths] and Tropical Rainfall Measurement Mission (TRMM) Microwave Imager (TMI; 700-km-wide swaths) overpasses in the years 1998–2001. Details of the imager and the retrieval algorithms are given by Wentz and Spencer (1998). The W, P, near-surface winds and column-integrated liquid water are simultaneously estimated using the brightness temperature observed at four frequencies (19.35, 22.235, 37, and 85.5 GHz). The retrieval algorithm is suitable for use only over ocean areas. The data were provided on a 0.25° × 0.25° grid. For analysis purposes, we first calculated a daily average at each ocean grid point based on all overpasses with valid data (typically 2–6), then averaged this daily data onto a 2.5° × 2.5° grid, retaining latitudes between 20°S and 20°N. We did not attempt to correct for possible sampling biases associated with the diurnal cycle.

As we discuss in the next section, we also found the daily averaged saturation water vapor path W_* to be a useful field. To compute W_*, we obtained twice-daily European Centre for Medium-Range Weather Forecasts (ECMWF) operational global temperature analyses at standard pressure levels from the Data Support Section of the National Center for Atmospheric Research (NCAR), from which we computed saturation specific humidity at each pressure level and grid point. We vertically integrated the saturation specific humidity and averaged over the two analyses each day to compute a daily average W_* at each grid point point. Because temperature above the boundary layer varies by only 1–2 K over the tropical oceans, and this variation occurs on broad space and time scales adequately sampled by the global atmospheric observation system, we assume this provides a fairly accurate determination of W_*.

3. SSM/I-derived relationships between P and W

a. Daily mean relationships

We first looked at the relation between daily averaged SSM/I P and W for all 2.5° × 2.5° ocean-covered grid boxes between 20°S and 20°N. A motivation for considering a daily time scale is that tropical oceanic convective precipitation averaged over a 2.5° × 2.5° area has an autocorrelation time scale on the order of a day. With some hindsight, this suggests that any universal nonlinear relationships between P and water vapor might emerge most clearly on this time scale. On longer time scales such relationships can get convolved with geographical or seasonal differences in the level of day-to-day humidity variability.

We compared four different tropical ocean regions shown in Fig. 1: the Indian Ocean, the west Pacific, the east Pacific, and the Atlantic Ocean. All include areas with 48-month-average rain rates exceeding 8 mm day^{-1}, as well as lightly precipitating areas.

For each region, all days in 1998–2001 at all locations were stratified into 1-mm water vapor path bins. Figure 2a compares the bin-averaged P for the four ocean regions. In all four regions, P increases rapidly with W. However, the west Pacific and Indian Ocean regions tend to have a smaller P for a given W (by up to 50% for W between 50 and 55 mm). Figure 2b shows the number of gridpoint months in each region for each W bin. Each region is well-represented in all W bins between 30 and 55 mm. Above $W = 55$ mm, the number of daily samples rapidly fall toward zero, especially in the Atlantic region.

The west Pacific/Indian Ocean region has a slightly higher mean tropospheric temperature than other parts of the tropical oceans. Following Raymond (2000), one might conjecture that a given intensity of convection will produce a universal relative humidity profile. This

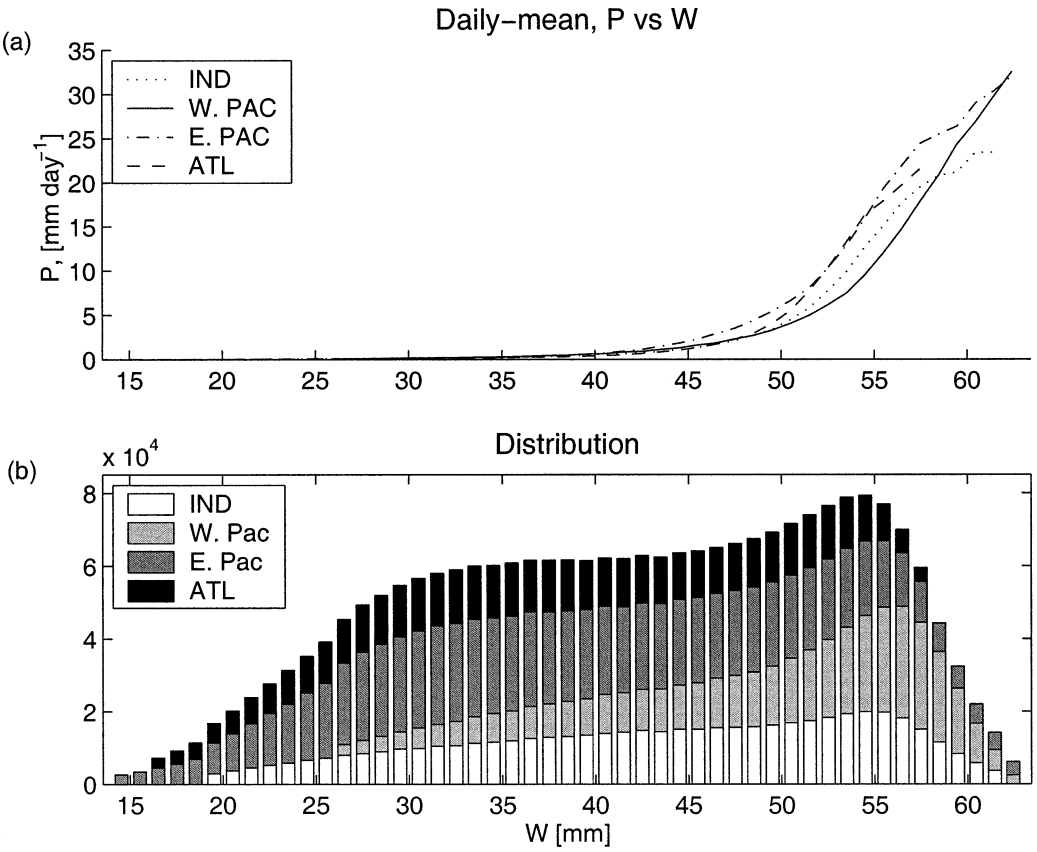

FIG. 2. (a) Mean daily averaged precipitation P in 1-mm-wide bins of water vapor path W, for the four tropical ocean regions in Fig. 1 for all months in 1998–2001. (b) Number of observations in each bin in the four regions.

would naturally lead to higher W for a given precipitation rate in the west Pacific and Indian Ocean compared to other ocean basins. With this conjecture in mind, we computed daily values of column-averaged relative humidity $r = W/W_*$, and sorted the data into bins of width 0.01 in r. Figure 3 shows bin-averaged P versus r. All four tropical ocean basins now more closely follow the same roughly exponential curve. In addition, all regions are now adequately represented in the humid tail of the distribution.

To quantify the r–P dependence, we compute the precipitation averaged over all grid points in all regions and days in each r bin with more than 2500 data points (this eliminates only the extreme ends). The crosses in Fig. 4 show the bin-mean precipitation. For every 5% increase in r, mean P more than doubles. We use a nonlinear least squares method to fit this with an exponential relationship of the form

$$P_d(r) = \exp[a_d(r - r_d)], \quad a_d = 15.6, \quad r_d = 0.603, \tag{1}$$

shown as the solid curve. This fit and all the results in Fig. 4 are of course dependent on the datasets used for r and particularly P. For instance, the 18-month-average of the Kwajalein radar-derived precipitation discussed in section 4 is about 30% less than the corresponding SSM/I-derived precipitation.

There is considerable variability about the mean r–P relationship. The 25th, 50th, and 75th percentiles of the daily P data for each r bin are plotted in Fig. 4 as dotted lines. The daily P has a skewed distribution in each bin (hence the mean substantially exceeds the median, lying roughly on the 65th percentile). The interquartile variability of P is roughtly a factor of 4 for the moist, heavily precipitating bins, and an even larger factor for the lightly precipitating bins. Some of this variability is real, but some may also reflect SSM/I sampling uncertainty. We will explore this issue using the Kwajalein radar dataset in section 4.

Another compelling demonstration of how daily precipitation is better related to r than to W is shown in Fig. 5. Figure 3 showed that using r in place of W removed regional differences in the water vapor path versus precipitation relationship. Figure 5 complements this by examining temporal variations in the water vapor path versus precipitation relationship in a persistently convecting location subject to substantial intraseasonal oscillations in tropospheric temperature and hence W_*. It compares daily time series of W and $0.8W_*$ for July–October 2001 from a grid point in the east Pacific ITCZ

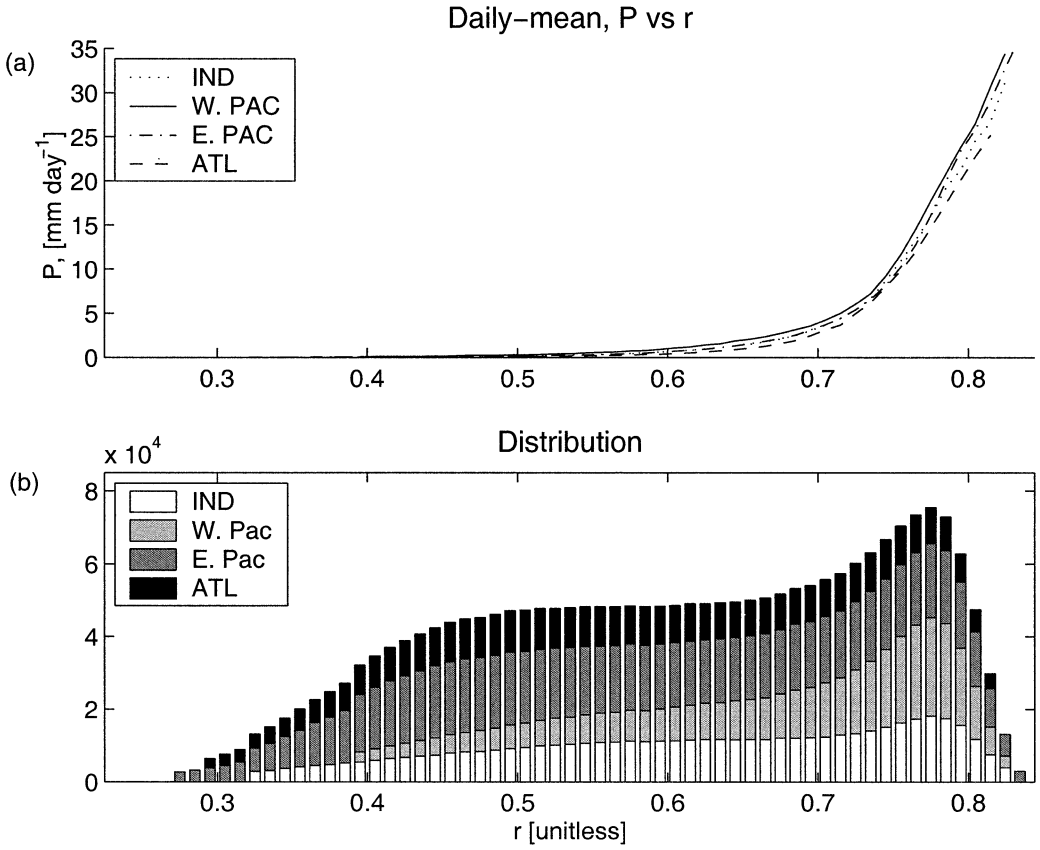

FIG. 3. (a) Mean daily averaged precipitation P in 1% bins of column-relative humidity τ, for the four tropical ocean regions in Fig. 1 for all months in 1998–2001. (b) Number of observations in each bin in the four regions.

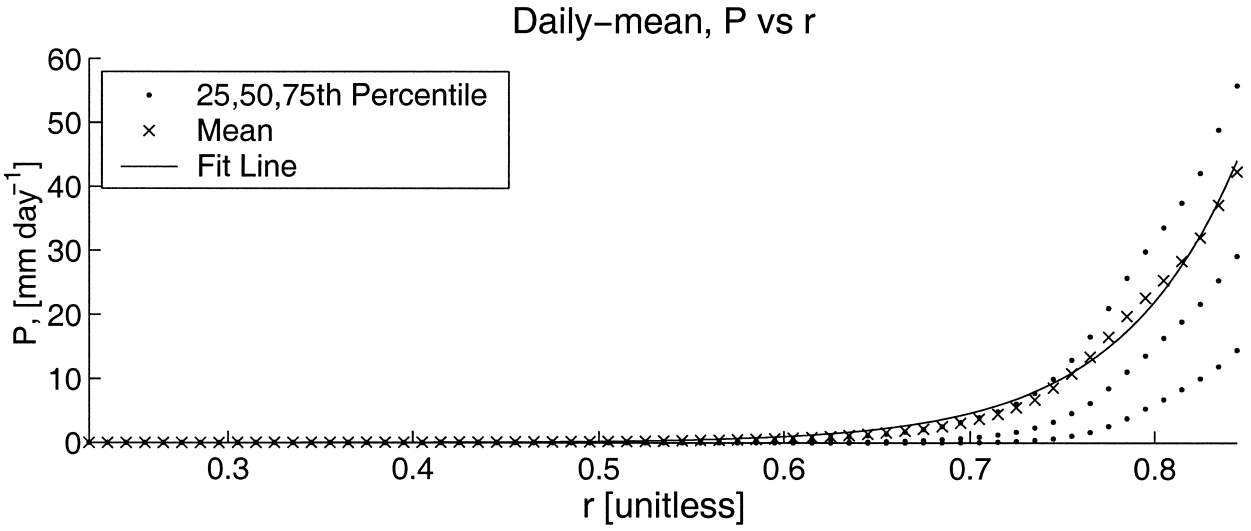

FIG. 4. Distribution of daily precipitation P in 1% bins of column-relative humidity r for all tropical ocean grid points in all months of 1998–2001. Dots show the 25th, 50th, and 75th percentiles of precipitation in each bin. The Xs show the bin-mean precipitation. The solid curve is the exponential fit (2).

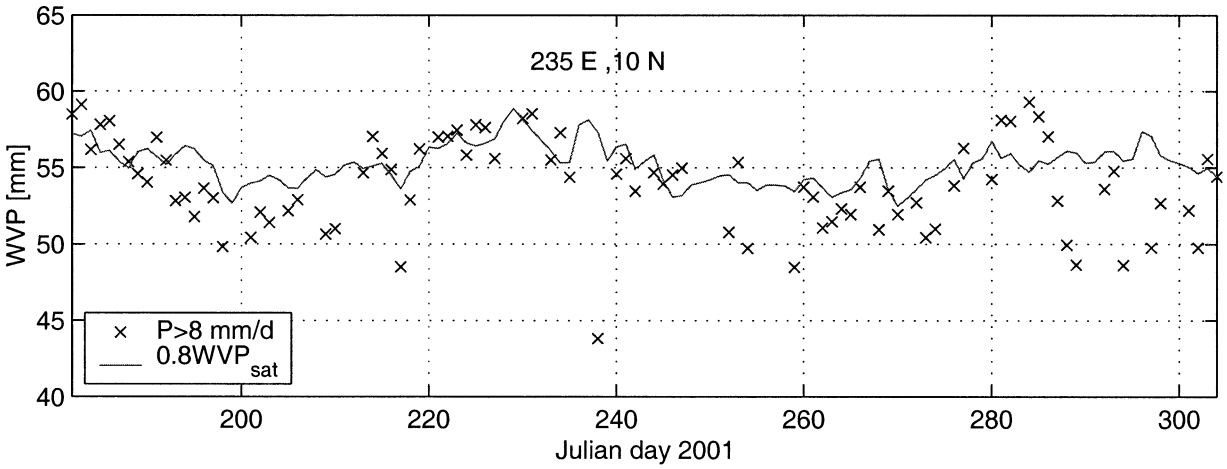

FIG. 5. Daily time series of SSM/I-derived W and ECMWF-derived $0.8W_*$ for Jul–Oct 2001 from a grid point in the east Pacific ITCZ (10°N, 125°W). SSM/I-derived W is only plotted on heavily precipitating days ($P > 8$ mm day^{-1}).

(10°N, 125°W). The W is only plotted on ''heavily precipitating'' days with P exceeding 8 mm day^{-1}. According to Fig. 4, these days should typically have $0.75 < W/W_* < 0.8$. In fact, their Ws predominantly lie just below the $W = 0.8W_*$ curve, and generally rise and fall in proportion to the intraseasonal variations in W_*. At this location, the low-frequency swings in W are slightly larger than those in $0.8W_*$. This suggests that the r–P relationship may have some slight but interesting spatiotemporal dependence, perhaps due to different thermodynamic conditions, wind shear and convective organization, stratiform/convective precipitation ratio, surface fluxes, etc.

b. Monthly mean relationships

The daily mean analysis can be repeated with monthly mean binning. As before, normalizing W into column-mean relative humidity r reduces systematic interbasin differences at high precipitation rates. The binned data, shown in Fig. 6, again can be fit by an exponential:

$$P_m(r) = \exp[a_m(r - r_m)], \quad a_m = 11.4, \quad r_m = 0.522. \tag{2}$$

The monthly mean fit $P_d(r)$ (solid curve) rises slightly less abruptly with monthly r than its daily counterpart (dashed curve). As one might expect, the monthly P has a less skewed distribution with a narrower spread between the 25th and 75th percentiles (±30% at high precipitation rates).

The monthly relation (2) between P and r can actually be derived from the corresponding daily relationship (1) as follows. For each day of a given month and every grid point, we can use the daily r to predict the daily P. We can then average the r and daily predicted P over the month. The bin average of the latter versus monthly average r almost exactly reproduces our monthly mean r–P relationship. In different regions, we find that the monthly r–P relationship varies slightly due to different levels of typical daily variability in r within individual months. To the extent that the r within a given fluid column only evolves ''slowly'' from day to day, so will its propensity to precipitate, that is, r may induce a weak day-to-day thermodynamic ''memory'' in P. However, P is sensitive to changes in r as small as a few hundredths, so precipitation, evaporation, and differential advection keep this memory quite short.

From our r–P relationships, we can define a convective moisture adjustment time scale τ_c for use in moist adjustment parameterizations of cumulus convection in simple models. A time scale derived from the monthly r–P relationship is appropriate for models of the quasi-steady seasonal tropical mean circulation such as the Quasi-equilibrium Tropical Circulation Model (QTCM) of Neelin and Zeng (2000) and simplifications thereof (e.g., Sobel 2003; Sobel and Gildor 2004). This is because these models typically do not explicitly simulate the large daily transients in convection. Instead they are tuned to produce a nearly steady-state solution that resembles a seasonal-mean climate and circulation. To derive such a time scale, suppose that r is increased from a typical reference value r_{ref} by a small amount δr, while column temperature changes insignificantly, so W_* remains constant. The increased r raises the precipitation rate by $\delta P = \delta r\, dP/dr(r_{\text{ref}})$. We define τ_c as the time scale over which the precipitation increase would remove the excess water vapor $\delta W = W_* \delta r$ from the column. Assuming reference values of saturation water vapor path $W_*^{\text{ref}} = 72$ mm and $r_{\text{ref}} = 0.72$ typical of regions of active tropical convection (the latter is the modal value of monthly mean r in the frequency plot in Fig. 6b), we obtain

$$\tau_c^m = \frac{\delta W}{\delta P} = \frac{W_*^{\text{ref}}}{dP_m/dr(r_{\text{ref}})} \approx 16 \text{ h}. \tag{3}$$

An analogous and slightly shorter convective moisture

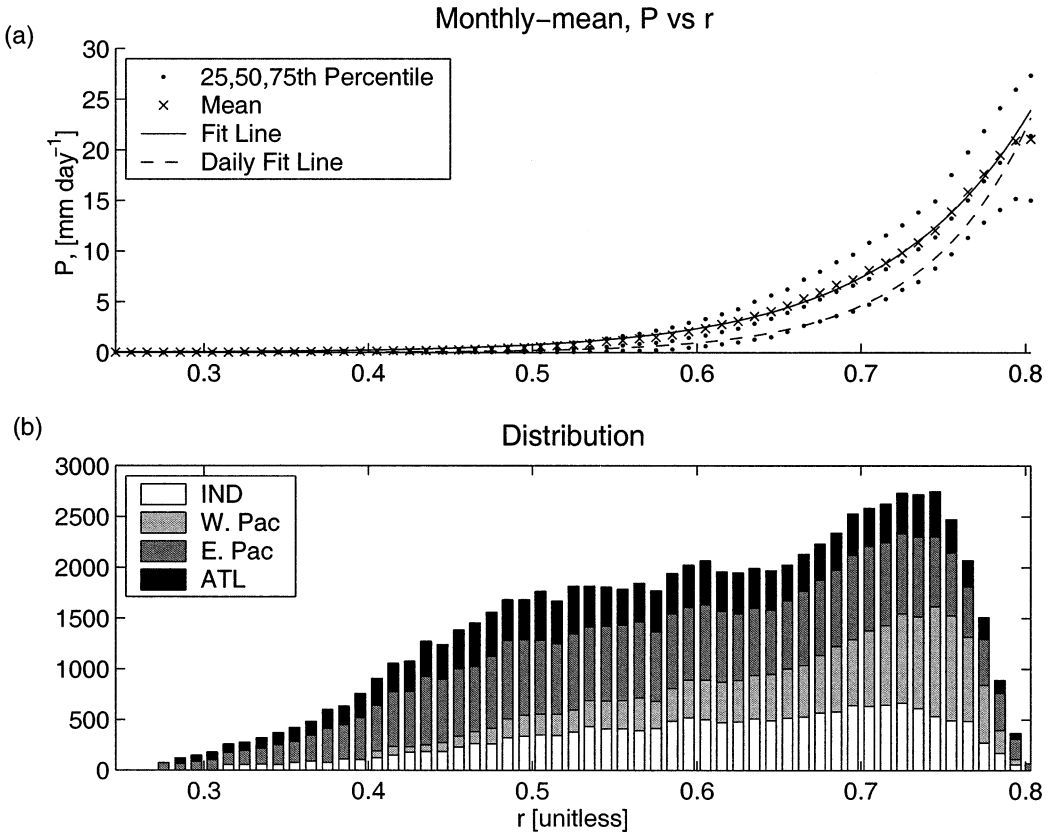

FIG. 6. (a) Distribution of monthly precipitation P in 1% bins of column-relative humidity r for all tropical ocean grid points in all months of 1998–2001. Dots show the 25th, 50th, and 75th percentiles of precipitation in each bin. The Xs show the bin-mean precipitation. The solid curve is the exponential fit (2) to the monthly data. For comparison, the dashed curve is the daily mean exponential fit (1). (b) Number of observations in each bin in the four regions.

adjustment time scale $\tau_c^d \approx 12$ h based on the daily r–P fit would be more appropriate if such a model were used to simulate convective variability on time scales of a few days. The time scale depends on r_{ref} and is shorter (longer) in a more (less) humid atmosphere.

c. Cross-spectral analysis

So far, we have established nonlinear relationships between r and simultaneous P on daily and monthly time scales. We performed a cross-spectral analysis to systematically examine how the relationship between P and r depends on the time scale, and to see if phase lags between r and P are apparent at any time scale. Cross-spectral analysis is a powerful tool, but unlike the binning analysis, cross-spectral analysis 1) requires filling in of missing data, and 2) detects only a linear fit, even if the underlying relationship is nonlinear.

Only ocean grid points with data for at least 98% of the days during the entire 4-yr period, including both the first or last day of the 4-yr period were used; this requirement only eliminated 3 of about 2000 grid points. At each grid point used, any days without data were filled in by linear interpolation in time.

Cross-spectral analysis is best used to compare variables whose anticipated relationship is roughly linear. We also wished to weight regions and seasons of persistent precipitation. Our approach was to construct a daily "r-predicted" precipitation time series $P_d(t)$ from the daily time series $r(t)$ at each grid point using (1). The anticipated relationship, which is linear, is that at each grid point

$$P(t) = P_d(t) + N(t), \tag{4}$$

where $N(t)$ is temporally uncorrelated white noise (with a noise amplitude that may depend on the signal amplitude P_d due to retrieval uncertainties and the physical dependence of precipitation on physical variables other than r). While a multiplicative noise model might be more physically plausible, the additive noise model has the advantage of de-emphasizing low-precipitation regimes where both our physical model and the satellite retrieval are suspect.

We computed a cross spectrum of P_d versus. P at each grid point as follows. The 4-yr means of P and P_d at each grid point were removed, then a cross-spectral estimate for that grid point was produced using a Hamming window of 365 days, overlapping successive win-

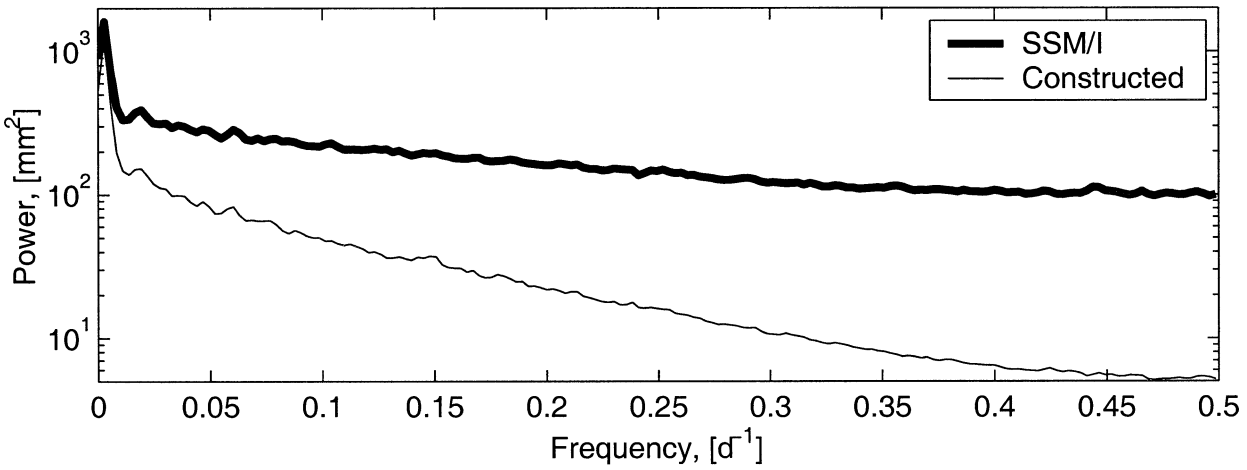

FIG. 7. Power spectra (mm^2) for precipitation P (thick black) and constructed precipitation P_d (thin black), averaged over all tropical ocean grid points.

dows by 182 days. These individual estimates were then averaged over all tropical ocean grid points into a single cross spectrum, from which the coherence, phase, and transfer function were obtained. This geographic averaging (justified by the apparent universality of the r–P relationship) greatly decreases the sampling noise in the spectral estimates. For an average over N statistically indistinguishable and independent grid points, the spectral estimate at each frequency is based on $4N$ independent data windows, because the 4-yr dataset has four fully distinct 365-day windows. Each of these windows contributes 2 degrees of freedom (dof). Even adjacent grid points have a low correlation between their daily precipitation rates (not shown here), so treating them as independent is not unreasonable. However, the effective dof will be somewhat reduced because the grid points are not statistically identical, and the spectral estimates will be weighted toward higher-variability, higher-precipitation regions. To roughly account for this, we estimated $N = 697$ based on the number of grid points with 4-yr precipitation greater than the tropical ocean mean of 4.83 mm day^{-1}.

The power spectra of P and particularly P_d (Fig. 7) are dominated by monthly and longer time scales, with the spectrum of precipitation rate P flattening toward white noise at higher frequencies. Figure 8a shows the coherence of P with P_d. At all sampled frequencies, this far exceeds the minimum coherence of 0.033 that is statistically significant at the 95% level based on $8N = 5776$ dof. As one might anticipate, the coherence increases at low frequencies, at which the effects of both retrieval uncertainties and other governing physical factors on daily P are averaged out.

The phase (Fig. 8b) is only barely distinguishable from zero statistically [simultaneous correlation of P with $P_d(r)$]. The slight hints of phase lags are region dependent.

Figure 8c shows that the real part of the transfer function $S_{P_dP}/S_{P_dP_d}$ is near 1 for all frequencies [$S_{AB}(f)$ denotes an estimated cross-spectral density between the time series $A(t)$ and $B(t)$ as a function of frequency f]. This is what we would expect from our statistical model (4), which would imply that the residual $N(t) = P(t) - P_d(t)$ is on average uncorrelated with $P_d(t)$, thus $S_{P_dP} = S_{P_dP_d} + S_{P_dN} = S_{P_dP_d}$. This supports our earlier contention that using daily r to predict daily $P_d(r)$ produces a precipitation time series that encompasses the SSM/I-observed relationship between r and P at all time scales.

d. *Vertical structure of monthly and geographical r–P covariability*

To understand the vertical structure of the monthly and geographical covariability of water vapor with precipitation, we obtained from J. Hack of NCAR a set of mean January, April, July, and October soundings from 24 tropical (20°N–20°S) sites that have long, high-quality data records (black squares in Fig. 1). These soundings were stratified by monthly mean precipitation, derived from the Xie and Arkin (1997) satellite-based climatology. We found $r = W/W_*$ is better correlated with P than is water vapor path W. Here, we try to identify the vertical moisture variations that lead $r = W/W_*$ to be correlated with P. To do this, we introduce a normalized specific humidity

$$q_n = (W_*^{\text{ref}}/W_*)q, \qquad W_*^{\text{ref}} = 72 \text{ mm}.$$

The mass-weighted vertical integral of q_n is proportional to column-relative humidity r. Using q_n in place of q corrects for small geographical and seasonal variations in tropospheric temperature that induce corresponding variations in W_*.

Figure 9 compares the profiles of q_n and relative humidity averaged over those mean soundings corresponding to 2–4, 4–8, and more than 8 mm day^{-1}. The higher-precipitation categories correspond to nearly uniform

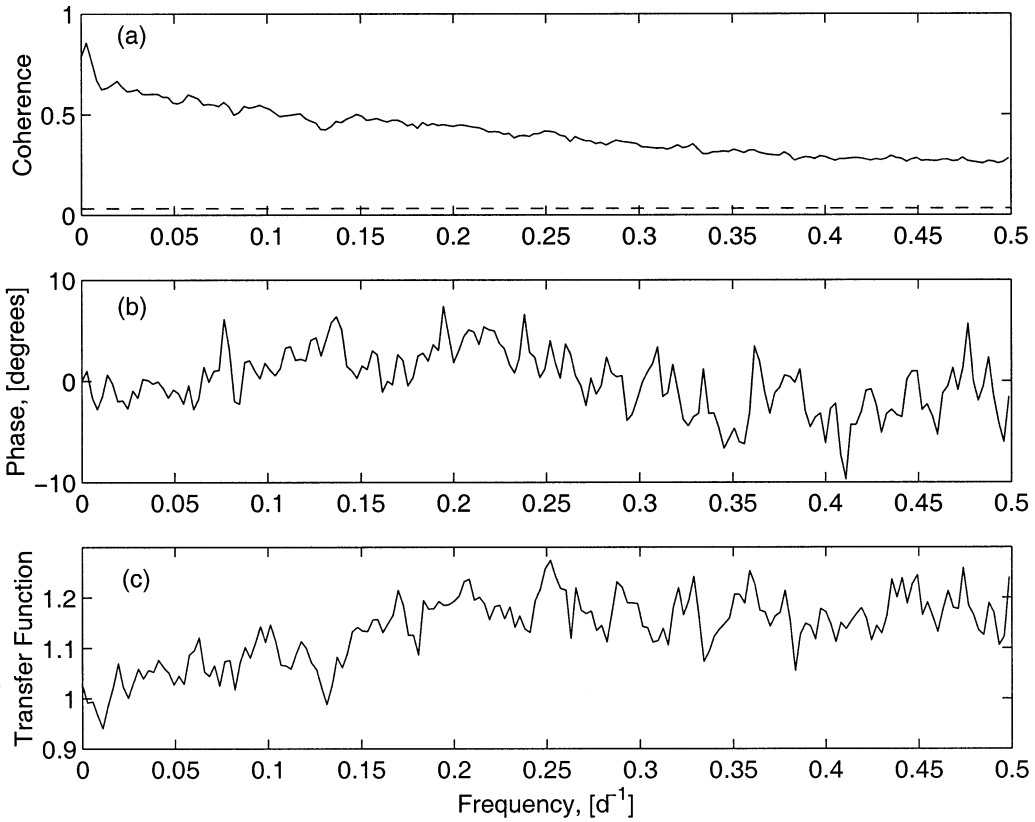

FIG. 8. Cross spectra of daily SSM/I P and $P_d(r)$: (a) coherence (dashed line demarcates the 95%-significance threshold), (b) phase, (c) real part of transfer function.

moistening between the surface and 500 mb; above this level the relative humidity perturbations remain large, but the q_n perturbations rapidly decrease. Even without normalizing by W_*, very similar results would be obtained. As expected from (2), a unit increase in monthly precipitation is associated with a much smaller increase in $q_n(p)$ in atmospheric columns that are already more moist and rainy than in drier columns.

e. Vertical structure of daily r–P covariability

We used radiosonde data from the TRMM Kwajalein Experiment (KWAJEX; 23 July–15 September 1999), together with coincident area-averaged precipitation derived from the TRMM C-band ground validation radar at Kwajalein, to determine how the vertical moisture profile varies with precipitation at a specific location at daily time scales. During KWAJEX, frequent soundings were taken at five sites within 150 km of Kwajalein Island (8.7°N, 167.7°W). Four of these sites were on very small islands; the other was a ship, so these soundings may be considered representative of an actively convecting region of the tropical ocean. As described by Sobel et al. (2004), the KWAJEX soundings were combined into a daily-mean all-site composite sounding, which is what we use here.

The Kwajalein radar made a volume scan every 10 min. For each scan, Houze et al. (2003, manuscript submitted to *J. Hydrometeor.*) derived rain maps with 2-km horizontal resolution out to 150-km radius around Kwajalein over a 6-month period using a carefully calibrated rainfall–reflectivity relationship. Beyond the 150-km range, the lowest elevation (0.5°) scans start near the freezing level of 4.5 km, which prevents this approach from being extended farther. These rain maps were area-averaged and daily averaged to derive area-averaged daily precipitation $P(t)$.

We binned the daily mean KWAJEX soundings into categories of P, and calculated average soundings of q_n for each category. We then subtracted the overall mean KWAJEX q_n sounding to get category-average perturbation soundings. Figure 10 shows the profiles of q_n and relative humidity perturbations for each category.

The profiles show a strong increase of q_n and relative humidity with precipitation rate in the midtroposphere. Below 900 mb, q_n is insensitive to P, presumably due to rapid turbulent interactions with a sea surface of nearly constant temperature. Again, almost identical results are obtained without normalizing by W_*.

The sensitivity of these vertical q_n profiles is somewhat different than was seen in the climatological soundings of Fig. 9, which included a range of locations

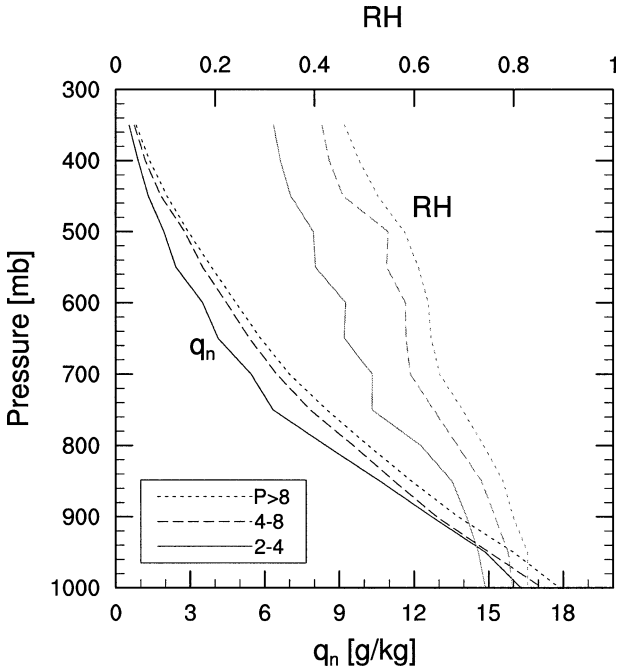

FIG. 9. Radiosonde-derived profiles of normalized monthly mean specific humidity (W^{ref}/W_*)q (left curves) and relative humidity (right curves), bin averaged by monthly mean Xie–Arkin precipitation (mm day^{-1}). The profiles are derived from Jan, Apr, Jul, and Oct climatologies at the 24 long-term radiosonde sites in 20°S–20°N shown in Fig. 1.

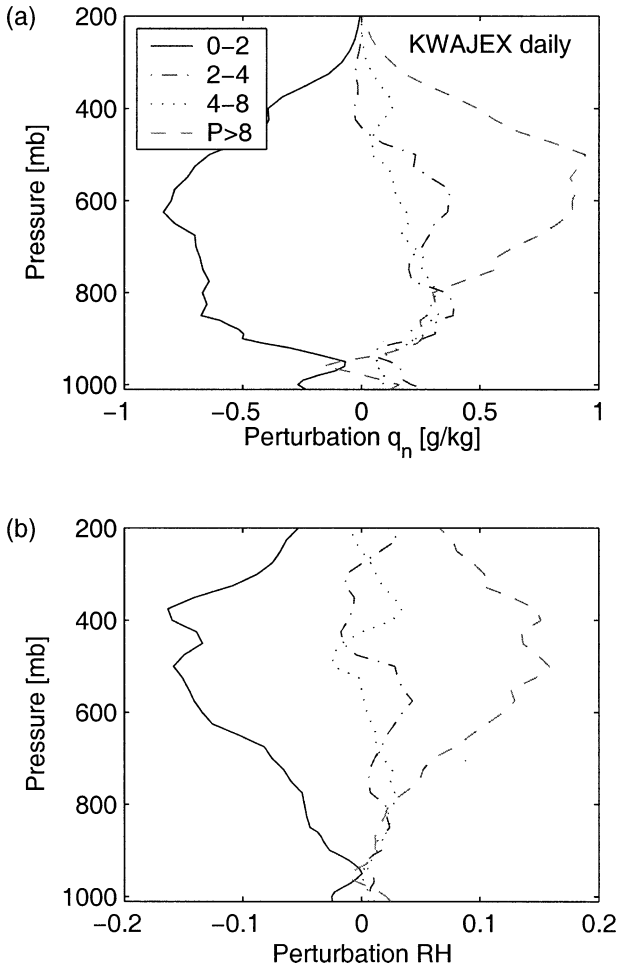

FIG. 10. Daily mean KWAJEX radiosonde-derived perturbation (a) normalized specific humidity and (b) relative humidity profiles bin averaged by daily mean radar-derived precipitation rate (mm day^{-1}).

spanning a range of sea surface temperatures (SSTs). In that case, there was a general correlation of SST with both P and near-surface q, so q_n shows a stronger near-surface dependence on P. If we had more sonde sites, or a reanalysis that had highly accurate humidity profiles, it would be interesting to stratify the climatological dataset into narrow SST ranges, then separately bin q_n against P for each SST to see if this removes the dependence of boundary layer q_n on P, producing a vertical profile more similar to the KWAJEX daily variations.

4. Validation using KWAJEX data

Passive microwave channels are well-suited to reliable determination of W (Staelin et al. 1976), except in localized regions of intense precipitation (which are probably anomalously moist, so could produce a small systematic underestimate of W if masked out to avoid contaminating the retrieval.) The retrieval of precipitation from SSM/I is more uncertain. The algorithm used by Remote Sensing Systems was designed to minimize cross talk among the retrieved parameters, and in particular to remove the water vapor contribution from the brightness temperature before computing the rain rate. Wentz (1997) showed the error in retrieved W (when compared against radiosonde soundings) is uncorrelated with the retrieved P. This suggests that significant correlations between W and P in our SSM/I dataset are unlikely to be due purely to the retrieval algorithm.

One may ask whether the retrieved P can really be used as a proxy for daily mean P on a 2.5° scale. There are large random retrieval errors inherent in the empirical algorithm to determine P for pixels in a given swath. Furthermore, the daily mean is derived from only 2–6 instantaneous swaths per day, and convection evolves rapidly. At a lesser level, the same concern also applies to W.

There is an extensive literature regarding errors in microwave precipitation retrievals (e.g., Wentz 1997; Kummerow and Giglio 1994) and undersampling biases (e.g., Morrissey and Janowiak 1996). However, there has been a dearth of long in situ radar datasets over the tropical ocean for validation; this has been a major TRMM motivation for maintaining the Kwajalein ground validation radar since 1999. Thus, we compared two area-averaged daily precipitation datasets derived from the Kwajalein radar with the daily SSM/I data. The first was the 150-km-radius dataset discussed in

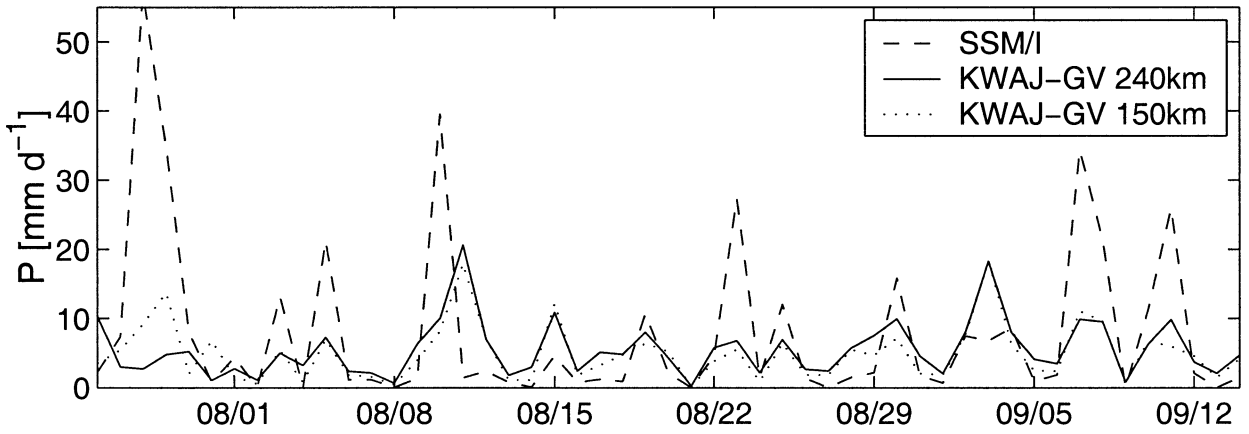

FIG. 11. Time series from 26 Jul to 14 Sep 1999 of Kwajalein radar-derived daily precipitation averaged over 150- and 240-km-radius circles and daily averaged SSM/I *P* over a collocated rectangular region of intermediate size.

section 3e, available for July–December 1999. The second was an estimate of precipitation area averaged over a larger 240-km-radius circle. This was derived using a cruder method (as described below), but was available for three Kwajalein rainy seasons (July–December, 1999–2001) instead of one, courtesy of Dr. S. Yuter. Every 10 min, the radar made an 0.5° elevation scan with a low pulse repetition frequency that extended its maximum range to 240 km. For each such scan, we estimated the area-averaged P (mm day^{-1}) over this 240-km circle as a constant multiple $c = 91$ of the area fraction $A(t)$ of this scan covered by echo exceeding 20 dB*Z*. The multiplier c was obtained by regressing this area fraction versus the simultaneous area-averaged precipitation derived by Houze et al. over the smaller 150-km circle for July–December 1999.

For comparison with these radar-derived precipitation datasets, the SSM/I data were averaged over the closest two 2.5° × 2.5° grid boxes to Kwajalein, centered at 8.75°N, 168.75°W, and 8.75°N, 166.25°W. This region contains most of the 150-km-radius circle centered on Kwajalein, but lies mainly inside the 240-km-radius circle.

Figure 11 shows this comparison for the KWAJEX period. The two radar datasets generally (though not invariably) track each other very closely, with a correlation coefficient exceeding 0.9 over July–December 1999, their overlap period. Hence, using exactly overlapping areas to compare area-averaged daily precipitation in this region appears not to be crucial. This justifies comparing the 240-km radar dataset with the two SSM/I grid boxes even though the two do not exactly span the same area. Also, use of the area-fraction method for precipitation estimation (for which we have the longer data record) appears adequately accurate for this work.

Figure 11 shows that SSM/I captures most of the heaviest daily rainfall events despite its temporal undersampling. It tends to significantly overpredict the large rain events (with considerable scatter) and underestimate the intervening light shower activity, with a roughly 40% overestimate of the time-mean precipita-

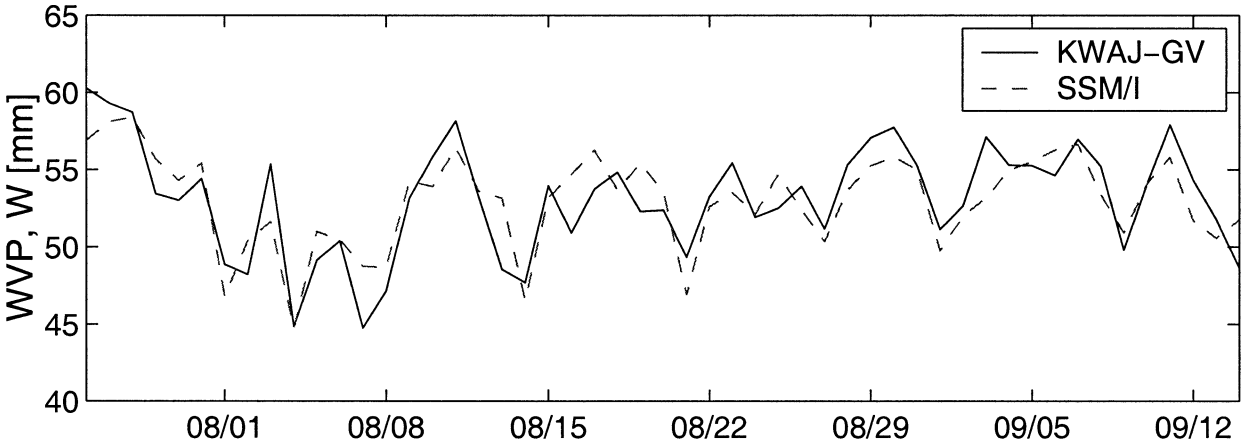

FIG. 12. Comparison of daily averaged KWAJEX all-site composite radiosonde and SSM/I water vapor path from 26 Jul to 14 Sep 1999.

tion compared to radar. Over the full 18-month comparison period, the correlation coefficient between the daily 240-km radar and SSM/I precipitation is 0.69 and a cross-spectral analysis shows coherence exceeding 0.5 (the 95% statistical significance level is 0.25) at all periods down to the Nyquist period of 2 days. At periods longer than 4 days the coherence is higher, 0.7 or more. This comparison gives us confidence that SSM/I-based precipitation in individual grid boxes is meaningful even down to periods of a few days.

Figure 12 shows a comparison over the same two months of daily W from SSM/I with rawinsonde observations from KWAJEX. Each daily sonde-derived water vapor path is an average of all sonde ascents (typically 15–30) during the day at four small islands and a ship, all scattered within 160 km of the Kwajalein radar each day (Sobel et al. 2004). Based on simultaneous comparisons between sites, we estimate the random sampling uncertainty in the daily average sonde water vapor path to be 0.7 mm. The correlation of SSM/I and sonde water vapor path over the KWAJEX period, 25 July–14 September 1999, was 0.82. Together, Figs. 11 and 12 lend credibility to SSM/I-derived relationships between P and W or r.

We used the 18 months of 240-km radar data to construct the distribution of daily radar-derived area-averaged P after binning by SSM/I-derived r, shown in Fig. 13a. Because both of these are comparatively accurate products, we hope this plot represents the true relationship of P to r on daily time scales and 300-km space scales better than if we used SSM/I-derived daily precipitation (Fig. 13b). The latter plot matches the global ocean r–P fit (1) quite well, confirming that the r–P relationship in the Kwajalein region is typical of the warm tropical oceans.

Figure 13a shows a slower increase of bin-mean P with r than Fig. 13b. This may reflect the SSM/I tendency to overestimate strong precipitation events while underestimating weak area-averaged precipitation rates around Kwajalein. There is also much less scatter (smaller 75th–25th percentile spread) of the radar-derived P about its bin mean than with the SSM/I P. Large random retrieval errors on the daily SSM/I P are likely artificially broadening its distribution for a given r. Figure 13c shows that we have sampled the range $0.7 < r < 0.8$ with at least 50 samples bin^{-1}. Signals at drier r, such as the secondary maximum of P at $r = 0.67$ seen in both Figs. 13a,b are uncertain due to inadequate sampling.

Although we have not done this, a somewhat similar analysis could be done over the global tropical ocean using the TRMM Precipitation Radar (PR) and TMI-derived r to build up a plot like Fig. 4. The TRMM sampling is less frequent and the PR footprint is much smaller than SSM/I, but the PR-derived rainfall is presumably more accurate than microwave estimates on daily time scales and is always obtained in a region simultaneously scanned by TMI.

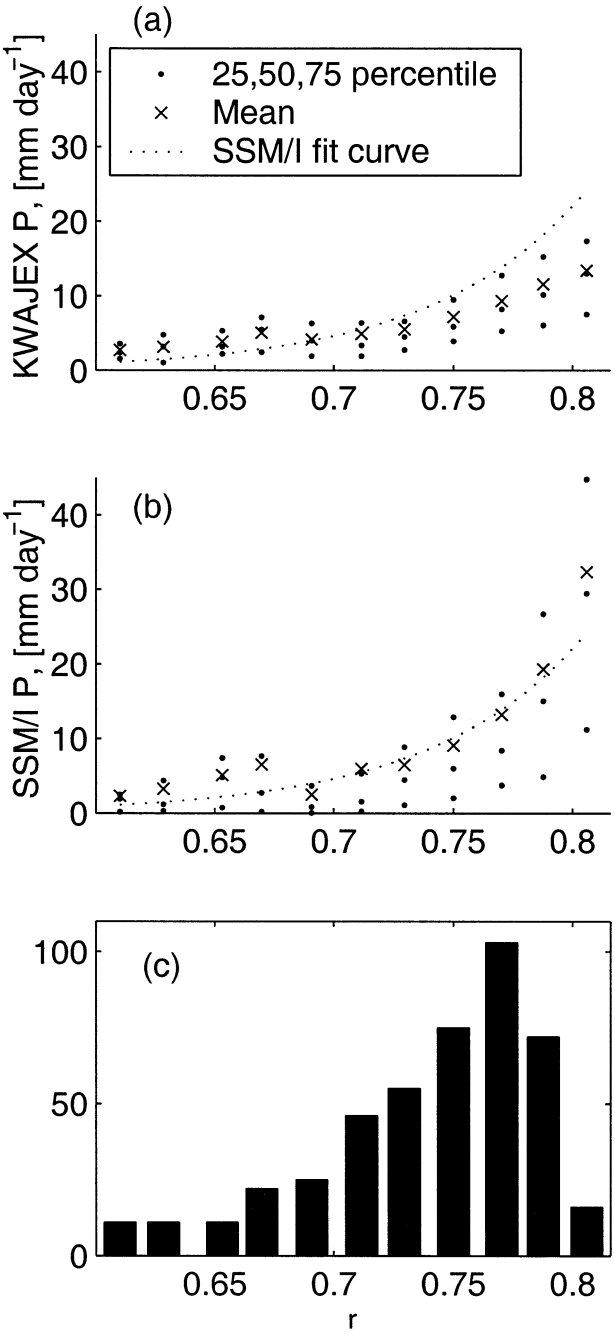

FIG. 13. (a) Daily 240-km radius area-averaged Kwajalein radar-derived precipitation for Jul–Dec 1999–2001 vs SSM/I-derived r, binned by r bins of width 0.02. Dots show the 25th, 50th, and 75th percentiles of precipitation in each bin. The Xs show the bin-mean precipitation. The dashed curve is the SSM/I-derived exponential fit (1); (b) as in (a), but with SSM/I-derived Kwajalein-area precipitation; (c) bin frequency.

5. Conclusions

Four years of daily SSM/I retrievals were used to look for relationships between tropical oceanic rainfall P and water vapor path W on daily to seasonal time scales.

Relationships that hold across all tropical ocean regions and seasons can be found if W is divided by the saturated water vapor path (derived from the column temperature profile) to obtain a column-relative humidity $r = W/W_*$. For monthly (''m'') and daily (''d'') data, these can be fit to the form $P_{m,d} = \exp[a_{m,d}(r - r_{m,d})]$; the choices of constants are different for daily than for monthly data. The scatter around these fits was characterized using plots of quartiles of the distribution of P in bins of r. The monthly fit can be obtained from the daily fit and the observed distribution of daily r found in a given month and location.

Cross-spectral analysis shows that at all periods from 2 to 180 days, P and the predicted daily $P_d(r)$ are almost exactly in phase, and are strongly correlated with almost no phase lag, though with more scatter at short, particularly at low frequencies. Radiosonde composites show the increased r at higher rainfall rates is due to a broad specific humidity increase between 400 and 850 hPa on daily time scales. The precipitation-related humidity anomalies extend down to the surface for monthly time scales.

That more convective rainfall should be associated with a more humid atmosphere is no surprise, but when quantified, this is an appealing test of convective parameterizations in weather and climate prediction models. In particular, it suggests that deep convective parameterizations that relax the humidity to a fixed reference profile [e.g., the Betts–Miller scheme (Betts 1986)] might perform better if the reference relative humidity profile were adjusted to be precipitation dependent. Alternatively, these schemes should use a moisture adjustment time scale τ_c of roughly 12 h for horizontal grid spacings on the order of 300 km, however, their temperature profile may be adjusted. This τ_c is much larger than the time scale of 1–2 h that has typically been used (Betts 1986).

Acknowledgments. This work was sponsored by NASA Grants NAGS5-10624 and NAG5-9657, and NSF Grant DMS-0139794. An earlier SSM/I dataset that got this work started was obtained from Chelle Gentemann of Remote Sensing Systems. The SSM/I dataset analyzed here was also obtained from Remote Sensing Systems, sponsored in part, by NASA's Earth Science Information Partnerships (ESIP): a federation of information sites for earth science; and by the NOAA/NASA Pathfinder Program for early EOS products; principal investigator: Frank Wentz. Dr. Sandra Yuter kindly provided us with 240-km echo area fraction time series for the Kwajalein radar scans. The radiosonde dataset was provided by James Hack and Mark Stevens of NCAR. Discussions with Dave Raymond helped inspire this work.

REFERENCES

Betts, A. K., 1986: A new convective adjustment scheme. Part I: Observational and theoretical basis. *Quart. J. Roy. Meteor. Soc.*, **112,** 677–691.

Brown, R. G., and C. Zhang, 1997: Variability of midtropospheric moisture and its effect on cloud-top height distribution during TOGA COARE. *J. Atmos. Sci.*, **54,** 2760–2774.

Johnson, R. H., and X. Lin, 1997: Episodic trade wind regimes over the western Pacific warm pool. *J. Atmos. Sci.*, **54,** 2020–2034.

Kummerow, C., and L. Giglio, 1994: A passive microwave technique for estimating rainfall and vertical structure information from space. Part II: Applications to SSM/I data. *J. Appl. Meteor.*, **33,** 19–34.

Morrissey, M. L., and J. E. Janowiak, 1996: Sampling-induced conditional biases in satellite climate-scale rainfall estimates. *J. Appl. Meteor.*, **35,** 541–548.

Neelin, J. D., and N. Zeng, 2000: A quasi-equilibrium tropical circulation model—Formulation. *J. Atmos. Sci.*, **57,** 1741–1766.

Numaguti, A., R. Oki, K. Nakamura, K. Tsuboki, N. Misawa, T. Aisai, and Y.-M. Kodama, 1995: 4–5-day-period variation and low-level dry air observed in the equatorial western Pacific during the TOGA-COARE IOP. *J. Meteor. Soc. Japan*, **73,** 267–290.

Raymond, D. J., 2000: Thermodynamic control of tropical rainfall. *Quart. J. Roy. Meteor. Soc.*, **126,** 889–898.

Sherwood, S. C., 1999: Convective precursors and predictability in the tropical west Pacific. *Mon. Wea. Rev.*, **127,** 2977–2991.

——, and R. Wahrlich, 1999: Observed evolution of tropical deep convective events and their environment. *Mon. Wea. Rev.*, **127,** 1777–1795.

Sobel, A. H., 2003: On the coexistence of an evaporation minimum and precipitation maximum in the warm pool. *J. Climate*, **16,** 1003–1009.

——, and H. Gildor, 2003: A simple time-dependent model of SST hot spots. *J. Climate*, **16,** 3978–3992.

——, S. E. Yuter, C. S. Bretherton, and G. N. Kiladis, 2004: Large-scale meteorology and deep convection during TRMM KWAJEX. *Mon. Wea. Rev.*, **122,** 422–444.

Staelin, D. H., K. F. Kunzi, R. L. Pettyjohn, R. K. L. Poon, and R. W. Wilcox, 1976: Remote sensing of atmospheric water vapor and liquid water with the *Nimbus 5* microwave spectrometer. *J. Appl. Meteor.*, **15,** 1204–1214.

Ushiyama, T., S. Satoh, and K. Takeuchi, 1995: Time and spatial variations of mesoscale rainfalls and their relation to the large-scale field in the western tropical Pacific. *J. Meteor. Soc. Japan*, **73,** 379–392.

Wentz, F. J., 1997: A well-calibrated ocean algorithm for SSM/I. *J. Geophys. Res.*, **102,** 8703–8718.

——, and R. W. Spencer, 1998: SSM/I rain retrievals within a unified all-weather ocean algorithm. *J. Atmos. Sci.*, **55,** 1613–1627.

Xie, P., and P. A. Arkin, 1997: Global precipitation: A 17-year monthly analysis based on gauge observations, satellite estimates, and numerical model outputs. *Bull. Amer. Meteor. Soc.*, **78,** 2539–2558.

Yoneyama, K., and T. Fujitani, 1995: The behavior of dry westerly air associated with convection observed during the TOGA-COARE R/V Natsushima cruise. *J. Meteor. Soc. Japan*, **73,** 291–304.

Zeng, X., 1999: The relationship among precipitation, cloud-top temperature, and precipitable water over the Tropics. *J. Climate*, **12,** 2503–2514.